

The interplay of electronic reconstructions, lattice distortions, and surface oxygen vacancies in insulator-metal transition of $\text{LaAlO}_3/\text{SrTiO}_3$

Jun Zhou,^{1,2,3} Teguh Citra Asmara,^{1,2,3} Ming Yang,^{1,2,3} George A. Sawatzky,⁴ Yuan Ping Feng,² and Andriwo Rusydi^{1,2,3,*}

¹*NUSNNI-Nanocore, National University of Singapore, Singapore 117542*

²*Department of Physics, National University of Singapore, Singapore 117542*

³*Singapore Synchrotron Light Source, National University of Singapore, Singapore 117603*

⁴*Department of Physics and Astronomy, University of British Columbia, Vancouver, Canada V6T1Z1*
(Dated: July 21, 2015)

The mechanism responsible for the extraordinary interface conductivity of LaAlO_3 on SrTiO_3 and its insulator-metal transition remains controversial. Here, using density functional theory calculations, we establish a comprehensive and coherent picture that the interplay of electronic reconstructions, lattice distortions, and surface oxygen vacancies fully compensates the polarization potential divergence in $\text{LaAlO}_3/\text{SrTiO}_3$, explaining naturally the experimental observations under different conditions. While lattice distortions and a charge redistribution between LaO and AlO_2 sub-layers play a dominant role in insulating state, a spontaneous appearance of $1/4$ oxygen vacancies per AlO_2 sub-layer at the LaAlO_3 surface accompanied by $0.5e^-$ charge-transfer into the interface is responsible for interface conductivity and the discontinuous transition in $\text{LaAlO}_3/\text{SrTiO}_3$. Our model also explain properties of $\text{LaAlO}_3/\text{SrTiO}_3$ prepared with different growth conditions.

I. INTRODUCTION

The interface of dissimilar oxide materials hosts rich varieties of exotic phenomena not found in its constituent materials and has attracted a tremendous amount of research interests, both for fundamental physics and practical applications¹⁻⁵. An ideal example is the interface of two different insulators, polar LaAlO_3 on nonpolar SrTiO_3 ($\text{LaAlO}_3/\text{SrTiO}_3$). In their bulk forms, both LaAlO_3 and SrTiO_3 are wide band gap non-magnetic insulators⁶. Remarkably, when a thin film of LaAlO_3 was deposited on SrTiO_3 , the interface was found to exhibit unusual phenomena such as a conducting two-dimensional electron gas (2DEG) with high mobility^{7,8}, superconducting⁹ and in some cases magnetic properties¹⁰⁻¹², and two-dimensional co-existence of both superconducting and magnetic properties^{13,14}. In particular, the fundamental phenomenon that has generated a lot of interests is the LaAlO_3 -thickness-dependent insulator-metal transition of $\text{LaAlO}_3/\text{SrTiO}_3$ interface. This phenomenon has several peculiar characteristics as shown by the various experimental observations summarized in Table I.

Recent high-energy reflectivity measurements have shown that in conducting $\text{LaAlO}_3/\text{SrTiO}_3$, a charge transfer of $0.5e^-$ from LaAlO_3 into $\text{LaAlO}_3/\text{SrTiO}_3$ interface and oxygen vacancies have been observed⁶. While in insulating $\text{LaAlO}_3/\text{SrTiO}_3$, an intra-layer charge redistribution within the LaAlO_3 film has been found. However, a fundamental mechanism to explain properties in insulating, conducting, as well as an important *step-function-shape* insulator-metal transition as a function of LaAlO_3 thickness in $\text{LaAlO}_3/\text{SrTiO}_3$ as one coherent picture is still lacking.

Previous theoretical studies¹⁵⁻²² discussed only some

of experimental observations (in Table I). For instance, calculations based on perfect $\text{LaAlO}_3/\text{SrTiO}_3$ structures^{17,18} or buckling¹⁵ did not describe at least two very important aspects observed in experiments. First, they did not explain the experimentally observed large discontinuity in the interface charge density as LaAlO_3 thickness increases above 4 unit cells (uc), but instead such calculations predicted this discontinuity only as a very gradual change. Second, the classical electronic reconstruction model and previous computational results would expect the surface of $\text{LaAlO}_3/\text{SrTiO}_3$ to also be metallic, which could strongly disrupt any conclusion drawn from transport and high-energy optical conductivity measurements regarding the interface charge density. Experimental observations instead show that the surface is insulating. Furthermore, recent first-principles calculations of a polarity-induced defect model²² were not adequate to explain important observations such as internal charge redistribution⁶ and lattice distortions^{23,24} of LaAlO_3 in insulating $\text{LaAlO}_3/\text{SrTiO}_3$.

Here, *via* first-principles calculations, we propose a unified picture that is an interplay of electronic reconstructions (both between LaAlO_3 sub-layers, and between LaAlO_3 and SrTiO_3), lattice distortions, and surface oxygen vacancies compensates the polarization potential divergence introduced due to the polar nature of LaAlO_3 , in different $\text{LaAlO}_3/\text{SrTiO}_3$ samples. Using this model, we are able to comprehensively explain the fundamental mechanism behind the observed physical properties (see Table I) as one coherent picture. Which of these mechanisms are dominant in a given thickness of LaAlO_3 are determined by the lowest total energy state in that particular set of conditions. We also show that our model can be applied to the $\text{LaAlO}_3/\text{SrTiO}_3$ prepared with different growth conditions, and other polar/nonpolar oxide

TABLE I. A list of fundamental experimental observations from various experimental methods of transport, high-energy optical conductivity, and structural features.

Observations for < 4 unit cells (uc) of LaAlO_3	
Electrical transport ⁶⁻⁸	1. The samples were all insulating.
High-energy optical conductivity ⁶	2. The samples were all insulating.
	3. A redistribution of $0.5e^-$ from AlO_2 sub-layer to LaO sub-layer has occurred.
	4. There was no inter-layer charge transfer into the interface.
Structural features ^{23,24}	5. No oxygen vacancies signature has been observed.
	6. An atomic buckling between cations and oxygen atoms was observed.
	7. These buckling decreased with increasing LaAlO_3 thickness.
Observations for ≥ 4 unit cells (uc) of LaAlO_3	
Electrical transport ⁶⁻⁸	8. SrTiO_3 exhibited an opposite buckling at the near-interface region, which increased with increasing layer thickness.
	9. The samples were all conducting.
	10. A sharp discontinuity of the electron gas density and insulator-metal transition at 4 uc LaAlO_3 has occurred.
High-energy optical conductivity ⁶	11. If LaAlO_3 thickness was further increased, the interface conductivity has remained relatively constant, independent of LaAlO_3 thickness.
	12. The surface of LaAlO_3 was always insulating.
	13. A decrease of $0.5e^-$ in LaAlO_3 film was observed.
Structural features ^{23,24}	14. It was accompanied by an increase of $0.5e^-$ at the interface, which resided in the SrTiO_3 side.
	15. Oxygen vacancies signature is observed in the LaAlO_3 film.
	16. The buckling for the Al site for 5 uc $\text{LaAlO}_3/\text{SrTiO}_3$ film was collapsed.

interfaces.

II. METHODOLOGY

All calculations were performed by using density-functional theory based on Vienna ab initio Simulation Package (VASP)^{25,26} with the Perdew-Burke-Ernzerhof (PBE) approximation for the exchange-correlation functional and the frozen-core all-electron projector-augmented wave (PAW) method for the

electron-ion interaction²⁷. The cutoff energy for the plane wave expansion was set to 400 eV. Gamma centered k-point grids for Brillouin zone sampling were set to $3 \times 3 \times 1$ for ionic relaxations and $6 \times 6 \times 1$ for static calculations, respectively. We used $2 \times 2 \times 1$ $\text{LaAlO}_3/\text{SrTiO}_3$ supercells for both stoichiometric structures and the structures with oxygen vacancies, the latter of which were created by removing one oxygen atom at the surface AlO_2 sub-layer of the stoichiometric $2 \times 2 \times 1$ $\text{LaAlO}_3/\text{SrTiO}_3$ supercells. The number of SrTiO_3 layers was fixed to 2 uc while the thickness of the LaAlO_3 film increased as 2, 3, 4, 5, and 6 uc. A much thicker (6uc) SrTiO_3 as substrate tested lead to similar results reported here. In order to minimize the interaction between neighbor surfaces, a 13 Å vacuum was applied along (001) plane of all interface structures. The lateral lattice constant of these supercells were fixed to 7.896 Å, twice as the equilibrium value of the bulk SrTiO_3 , in good agreement with previous studies^{19,21}. All the atoms except the bottom SrO sub-layer were allowed to relax until the forces are smaller than 0.02 eV/Å. Since SrTiO_3 is not a polar material, the dipole field, if any, must be quite small. To avoid the spurious electric field, dipole corrections were included. Calculations on the density of states of $\text{LaAlO}_3/\text{SrTiO}_3$ were performed, confirming that there is no mid-gap state being introduced at the bottom of SrO sub-layer. The internal electric field in LaAlO_3 was calculated by the slope of macroscopically averaged electrostatic potentials²⁸.

The formation energy of the surface oxygen vacancies is defined by³¹:

$$E_f = E_{total} - E_{host} + \mu(T, P),$$

where E_{total} is the calculated total energy of slabs with oxygen vacancies, E_{host} the energy for the stoichiometric $2 \times 2 \times 1$ supercells, and $\mu(T, P)$ is the chemical potential of oxygen, which is related with sample growth environment. Experimentally, the upper limit of oxygen partial pressure for layer-by-layer epitaxial growth of LaAlO_3 films on SrTiO_3 is 5×10^{-2} mbar, while the lower limit is 1×10^{-6} mbar at the growth temperature of 850 °C¹¹. With these data, we calculate the corresponding energy of the upper and lower oxygen chemical potential to be -6.77 eV and -7.18 eV, respectively.

III. RESULTS AND DISCUSSIONS

To investigate the structural and electronic properties of stoichiometric 2, 3, 4, 5, and 6 uc LaAlO_3 layers on an SrTiO_3 substrate, we perform density functional theory (DFT) calculations on the thickness dependence of charge density at the interface, averaged lattice distortions of O-La-O and O-Al-O chains, and remnant internal electric field in LaAlO_3 layers. As shown in Fig. 1a, there is an insulator-metal transition between 4 and 5 uc $\text{LaAlO}_3/\text{SrTiO}_3$. For the conducting cases, the charge density at the interfaces increases monotonically with d_{LaAlO_3} . The lattice distortions between O and cationic

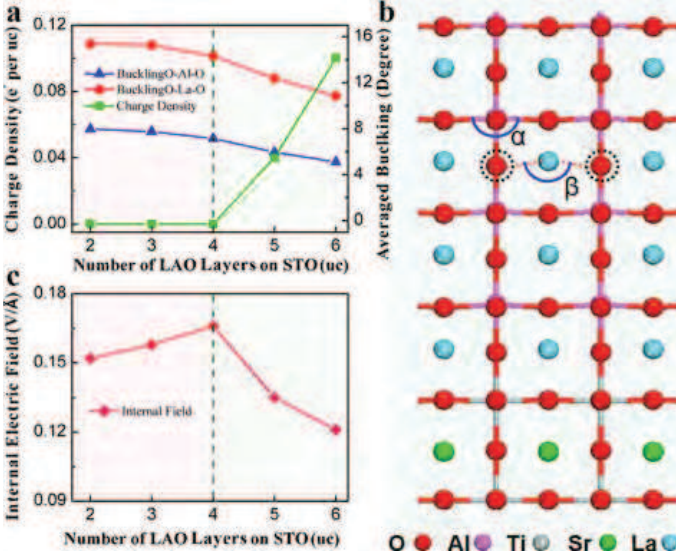


FIG. 1. Insulator-metal transition and lattice distortions in stoichiometric $\text{LaAlO}_3/\text{SrTiO}_3$. (a) LaAlO_3 thickness dependence of charge density at the interface, along with the average buckling of La-O-La and O-Al-O chains in LaAlO_3 films. To study the thickness-dependence behavior, we average the angles defined by $180^\circ - \alpha$ and $180^\circ - \beta$ for O-Al-O and O-La-O chains respectively, where α and β are shown in Fig.1(b). (b) Structural guide for the buckling of O-Al-O and O-La-O chains. We should note that the circled oxygen atoms is not in the same plane with La atoms but we define their angle β as the projected in-plane angle between their buckling. (c) The remnant electric field in LaAlO_3 films of $\text{LaAlO}_3/\text{SrTiO}_3$ at different LaAlO_3 thicknesses.

atoms (as defined in Fig. 1b) are found in LaAlO_3 film of all thicknesses. Overall, the lattice distortions of O-La-O chains are more pronounced than the lattice distortions of O-Al-O chains, consistent with experimental observations²³. These cationic displacements introduce dipoles opposite to the polar electric field of LaAlO_3 , and thus partially compensates it, leaving a remnant electric field in LaAlO_3 .

Fig. 1(c) shows the remnant electric field after partial compensation by the lattice distortions and electronic reconstructions. It can be seen that, below 5 uc of LaAlO_3 , the lattice distortions cannot fully compensate the polar electric field, as the remnant electric field keeps increasing with the increase of d_{LaAlO_3} . When the $d_{\text{LaAlO}_3} > 4$ uc, a critical point is reached and the remnant electric field results in a potential difference that exceeds the LaAlO_3 band gap, which causes an internal Zener breakdown to occur. At this point, electronic reconstruction happens in $\text{LaAlO}_3/\text{SrTiO}_3$ via electrons transfer from surface AlO_2 sub-layer into interface TiO_2 sub-layers, leaving extra holes at surface AlO_2 and extra electrons at interface TiO_2 sub-layers, although the calculated charge density remains very small. We note that the phenomenon of electronic reconstruction was introduced in earlier study of polar surfaces in K_3C_{60} ²⁹. This electronic reconstruc-

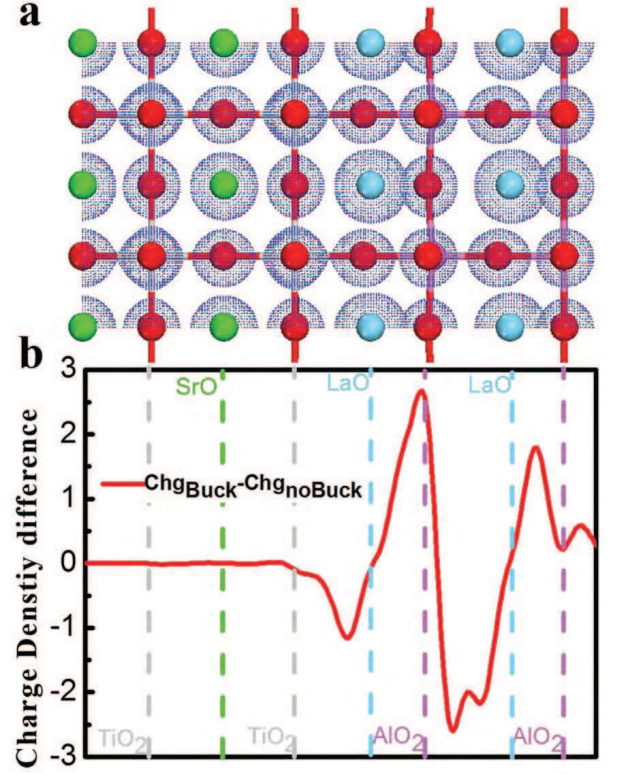


FIG. 2. In-plane averaged charge density of stoichiometric 2 uc $\text{LaAlO}_3/\text{SrTiO}_3$. (a) Structural configuration of stoichiometric 2 uc $\text{LaAlO}_3/\text{SrTiO}_3$ and the corresponding charge density distribution (isovalue = 0.027 $\text{e}/\text{\AA}^3$). (b) Difference of the xy-plane-averaged electron density between relaxed and unrelaxed cases.

tion also compensates the polar electric field of LaAlO_3 , leading to a sharp decrease of the remnant electric field after 4 uc of LaAlO_3 (see Fig. 1c).

Recent high-energy optical conductivity measurement of $\text{LaAlO}_3/\text{SrTiO}_3$ shows that there is charge redistribution between LaO and AlO_2 sub-layers in insulating $\text{LaAlO}_3/\text{SrTiO}_3$ ⁶. In Fig. 2, we compare the charge density distribution between relaxed and unrelaxed stoichiometric 2 uc $\text{LaAlO}_3/\text{SrTiO}_3$ structures and the internal charge redistribution between LaAlO_3 sub-layers is indeed found in our calculations. Because of the lattice distortions, the La atoms move upwards to the surface while the oxygen atoms in AlO_2 sub-layers move downwards to the interface (the La-O buckling dipole), making their orbitals more overlapped and thus more covalent than in the structures without lattice distortions. Although the overlap between Al atoms in AlO_2 sub-layers and the oxygen atoms in LaO sub-layers (the Al-O buckling dipole) counteracts the charge redistribution caused by the La-O buckling dipole, this effect is inferior due to the less pronounced lattice distortions of O-Al-O chains than the O-La-O chains. Since this internal LaAlO_3 charge redistribution has strong interplay with the lattice distortion effects, it also disappears once the

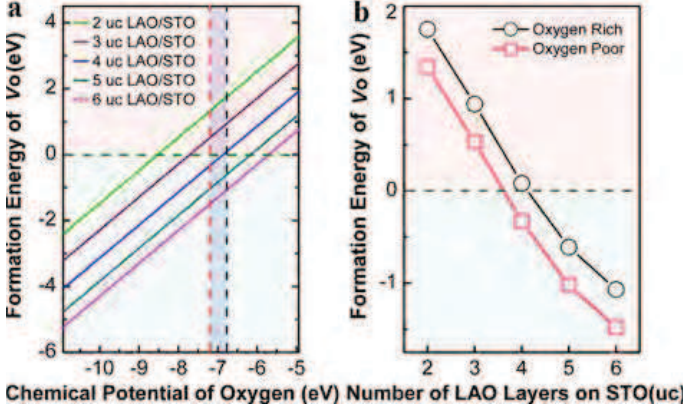


FIG. 3. Formation energy of surface oxygen vacancies in LaAlO₃/SrTiO₃ with different oxygen chemical potential and LaAlO₃ thicknesses. (a) Oxygen chemical potential dependence of formation energy of surface oxygen vacancies in LaAlO₃/SrTiO₃. The vertical black dash line indicates the oxygen rich condition, while the vertical red dash line indicates the oxygen poor condition. (b) The formation energy of surface oxygen vacancies for experimental oxygen-rich and oxygen-poor conditions as a function of LaAlO₃ thicknesses dependence in LaAlO₃/SrTiO₃.

atomic lattice distortions vanish. For this stoichiometric 2 uc LaAlO₃/SrTiO₃ structure, there is no charge redistribution between LaAlO₃ and SrTiO₃, consistent with experimental observations⁶.

Up to this point, we are able to explain to some extent the experimental observations of insulating LaAlO₃/SrTiO₃ (2 and 3 uc LaAlO₃/SrTiO₃), *i.e.* the electronic redistribution inner LaAlO₃ sub-layers⁶, the lattice distortions^{23,24}, and the remnant electric field³⁰. However, this stoichiometric LaAlO₃/SrTiO₃ model is not able to fully explain the conducting LaAlO₃/SrTiO₃. First, the critical LaAlO₃ thickness happens at 5 uc instead of 4 uc as observed experimentally⁸. Second, in conducting samples, the charge density increases with LaAlO₃ thickness, while experimentally the charge density of conducting LaAlO₃/SrTiO₃ is independent from LaAlO₃ thickness, as observed in the step-like insulator-metal transition^{6,8}. Third, the charge density is much less than the $0.5e^-$ observed experimentally⁶. Fourth, the lattice distortions still remain after the interface becomes conducting, while experimentally^{23,24} they collapse in conducting LaAlO₃/SrTiO₃.

Another important observation in high-energy optical conductivity of LaAlO₃/SrTiO₃ measurement was that the conducting LaAlO₃/SrTiO₃ exhibited V_O signature in LaAlO₃.⁶ However, this signature was not observed in insulating LaAlO₃/SrTiO₃. This suggests that the formation conditions for V_O in insulating and conducting LaAlO₃/SrTiO₃ are different. For this reason, we calculate formation energy (E_f) of V_O in LaAlO₃ film of LaAlO₃/SrTiO₃ with different LaAlO₃ thicknesses. First of all, our calculations show that in LaAlO₃ film, the E_f

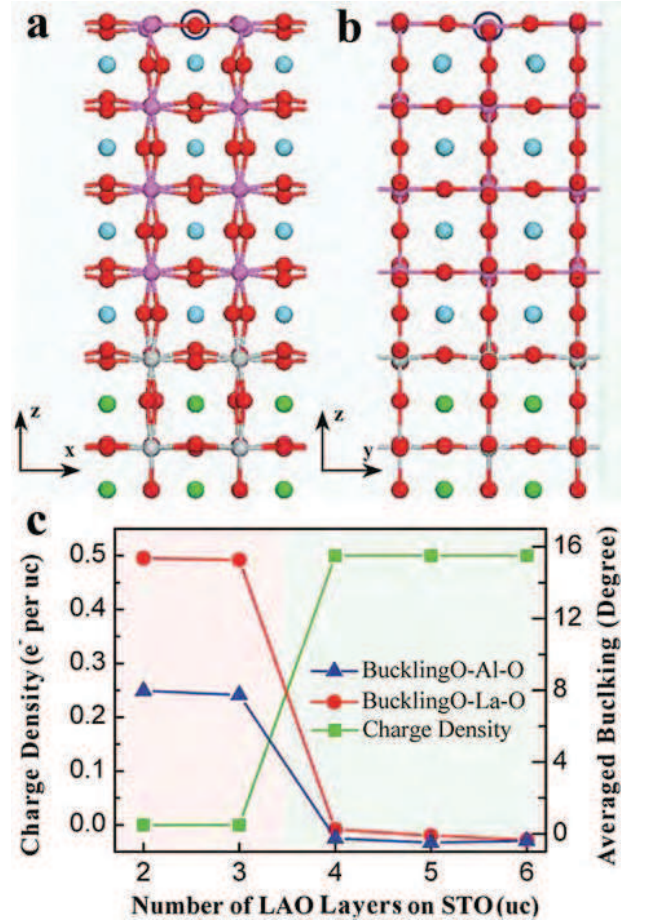


FIG. 4. Insulator-metal transition and lattice distortions in LaAlO₃/SrTiO₃, after the introduction of surface oxygen vacancies in conducting LaAlO₃/SrTiO₃. (a) Structural guide for the relaxed 4 uc LaAlO₃/SrTiO₃ along $\langle 010 \rangle$ direction with surface oxygen vacancy. (b) Structural guide for the relaxed 4 uc LaAlO₃/SrTiO₃ along $\langle 100 \rangle$ direction with surface oxygen vacancy. (c) LaAlO₃ thickness dependence of number of excess charge at the interface, and the average buckling of La-O-La and O-Al-O chains in LaAlO₃ thin films for different thicknesses of LaAlO₃ on SrTiO₃. The 2 and 3 uc LaAlO₃/SrTiO₃ are stoichiometric, while the 4, 5, and 6 uc LaAlO₃/SrTiO₃ are with surface oxygen vacancies.

of V_O is the lowest at the surface. Secondly, the E_f of surface V_O in LaAlO₃/SrTiO₃ also varies as a function of LaAlO₃ thickness and oxygen chemical potential, as shown in Fig. 3. One clearly sees that E_f of surface V_O decreases as the thickness of LaAlO₃ increases, which means it is more energetically favorable to create surface V_O in thicker LaAlO₃ film. Interestingly, when $d_{LaAlO_3} \geq 4$ uc, the formation energy of surface V_O crosses through zero at most oxygen chemical potential window, indicating a high possibility to form the surface V_O .

Experimentally, the upper limit of oxygen partial pressure for layer-by-layer deposition of LaAlO₃/SrTiO₃ is 5×10^{-2} mbar with a typical deposition temperature

of 850 °C¹¹, implying this oxygen partial pressure is the oxygen-rich limit of LaAlO₃/SrTiO₃ deposition. The calculated formation energy of surface oxygen at this oxygen chemical potential is shown in Fig. 3b. It can be seen that formation energy is equal to or below zero for $d_{\text{LaAlO}_3} \geq 4$ uc, even at this oxygen-rich limit, suggesting that the oxygen vacancies are energetically favorable to be formed in LaAlO₃ film with these thicknesses.

Based on this reason, we perform DFT calculations by including surface V_O for 4, 5, and 6 uc LaAlO₃/SrTiO₃, which are experimentally found to be conducting⁸. The relaxed LaAlO₃/SrTiO₃ structure after the inclusion of surface V_O is shown in Fig. 4a,b along different directions. From here, the dipole-inducing lattice distortions as defined in Fig. 1b vanish, consistent with experimental results^{23,24}. The lattice distortions seen in Fig. 4a and 4b are mainly caused by the absence of one surface oxygen atom in 2×2×1 supercell, and do not give rise to cationic dipoles.

The results of the calculations for the charge density are also shown in Fig. 4c. (Note that the calculations for the charge density and buckling in 2 and 3 uc LaAlO₃/SrTiO₃ are performed without including surface V_O , the same as the results in Fig. 1a.) It can be seen that the LaAlO₃ thickness dependence of the interface charge density now forms a step function, resulting in a discontinuity transition, consistent with experimental observations^{6,8}. There are four main effects of surface V_O . First, the charge density is found to be 0.5e⁻, which completely compensates the polar electric field, consistent with the experimental observation⁶. Second, the amount of 0.5e⁻ is consistent with the inter-layer charge transfer stipulated by the electronic reconstruction model. Third, the 0.5e⁻ charge density is independent of LaAlO₃ thickness (and results in an insulating surface), also in good agreement with experimental results^{6,8}. Fourth, we can reconcile the presence of surface V_O with the reconstruction model for polar crystal terminations, as discussed below.

In the conventional electronic reconstruction model²⁹, without allowing for V_O or the internal lattice distortions described above, the charge of 0.5e⁻ at the interface is compensated by 0.5 holes in the mainly O-2p band of the AlO₂-terminated surface of LaAlO₃. In this model not allowing for lattice distortions or other deviations the electronic reconstruction would occur immediately after even only one layer of LaAlO₃ was deposited (see Fig. 5a), contrary with experimental observations^{6,8}. Even more importantly, both the SrTiO₃ interface layer and the top AlO₂ surface layer would become metallic. Allowing for the lattice distortions, as shown in Fig. 5b, demonstrates that these internal distortions can compensate for the internal polarization potential divergence for $d_{\text{LaAlO}_3} < 4$ uc, without electronic reconstruction into the interface. Meanwhile, for $d_{\text{LaAlO}_3} \geq 4$ uc the top of the valence band of LaAlO₃ and the bottom of the conduction band of SrTiO₃ starts to overlap. These result in both the interface and the surface becoming metallic with a very

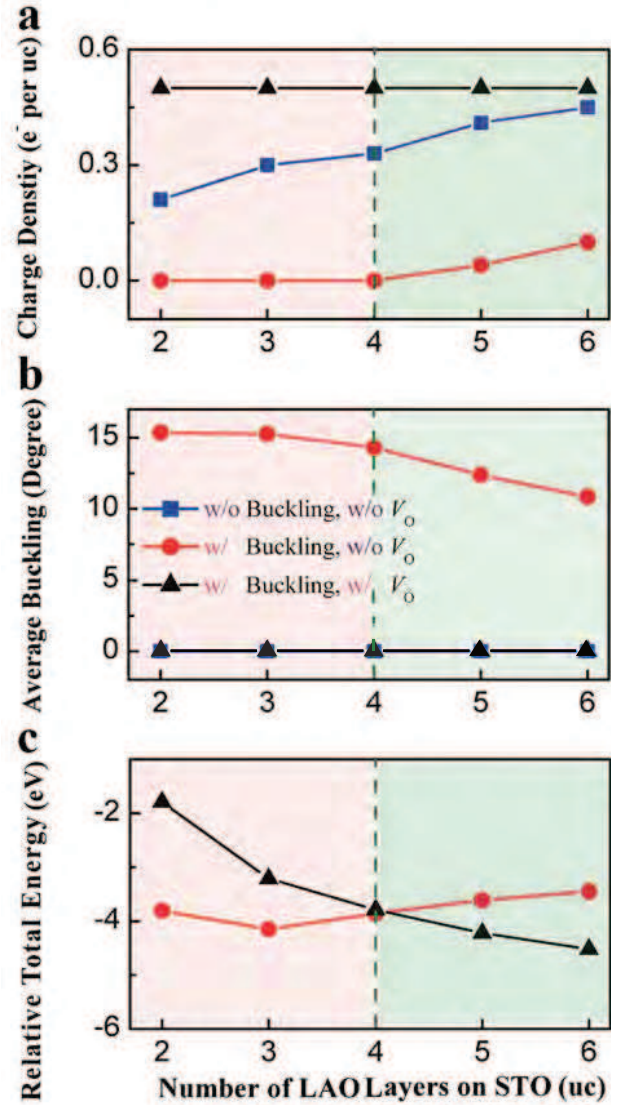


FIG. 5. A discontinuity phase-like transition due to interplay of electronic reconstructions, lattice distortions, and surface oxygen vacancies. Three cases of LaAlO₃/SrTiO₃ are considered: (1) LaAlO₃/SrTiO₃ without both lattice distortions and surface oxygen vacancies (blue squares), (2) LaAlO₃/SrTiO₃ with lattice distortion but without surface oxygen vacancies (red circles), and (3) LaAlO₃/SrTiO₃ with both lattice distortion and surface oxygen vacancies (black triangles). (a) Comparison of the interface charge density of each case. (b) Comparison of O-Al-O chains buckling in LaAlO₃ film of each case. (c) Comparison of relative total energy of the second and third cases, with the first case as the reference. Below 4 uc LaAlO₃ film (red-shaded region), the second case results in the lowest total energy and is consistent with experimental observations^{6,8,23}. On the other hand, above 4 uc LaAlO₃ film (green-shaded region) it is the third case that results in the lowest total energy and agreement with experimental observations^{6,8,23}.

small but gradually increasing charge density of opposite sign as the LaAlO_3 thickness increases (see Fig. 1a and 5a).

The energy to create V_O , however, approaches zero at 4 uc of LaAlO_3 (Fig. 3) and becomes negative as LaAlO_3 thickness is further increased. In this case, the total energy of the system with $1/4 V_O$ per AlO_2 sub-layer and reduced lattice distortions is lower than the total energy for the case without the surface V_O and with the strong lattice distortions. Thus, this becomes the energetically favorable situation (see Fig. 5c). This results in $0.5e^-$ at the interface, while the top AlO_2 sub-layer remains insulating because the electrons left behind by the formation of V_O are transferred to the interface. In this way the sample as a whole remains charge neutral as must be the case.

Based on these results, our model can naturally explain the LaAlO_3 -thickness-dependent discontinuous transition at 4 uc LaAlO_3 of $\text{LaAlO}_3/\text{SrTiO}_3$. Below 4 uc of LaAlO_3 , the internal polarization potential in LaAlO_3 is compensated by the lattice distortions of LaAlO_3 film without electronic reconstruction into the interface accompanied by the intra-layer charge redistribution within the LaAlO_3 film, resulting in insulating $\text{LaAlO}_3/\text{SrTiO}_3$. Above 4 uc of LaAlO_3 , the internal polarization potential in LaAlO_3 is instead compensated by electronic reconstruction into the interface, stabilized by the energetically favorable spontaneous appearance of V_O in the surface AlO_2 sub-layer of LaAlO_3 , resulting in conducting $\text{LaAlO}_3/\text{SrTiO}_3$ interface with LaAlO_3 -thickness-independent charge density.

Furthermore, we can classify three types of $\text{LaAlO}_3/\text{SrTiO}_3$ samples based on different experimental conditions^{8,32–34}. First, when the LaAlO_3 film is deposited on SrTiO_3 with moderate oxygen partial pressure, surface V_O forms, which leads to the insulator to

metal behavior of $\text{LaAlO}_3/\text{SrTiO}_3$ described in Fig. 4c. Second, when this $\text{LaAlO}_3/\text{SrTiO}_3$ is post-annealed in high oxygen pressure, the experimentally-observed conductivity decreases, but is not completely gone^{8,33,34}. Based on our model, this suggests that the oxygen annealing removes some of the surface V_O , leading to the insulator-metal transition behavior of stoichiometric $\text{LaAlO}_3/\text{SrTiO}_3$ described in Fig. 1a with its much lower interface charge density. Third, when LaAlO_3 is deposited with very low oxygen pressure, it is experimentally observed that the conduction region of $\text{LaAlO}_3/\text{SrTiO}_3$ extends up to $500 \mu\text{m}$ ³². This suggests that the low oxygen pressure condition generates a high number of V_O in SrTiO_3 (instead of surface LaAlO_3), giving rise to three-dimensional electron gas at the interface³².

In conclusion, our result shows that interplay of electronic reconstructions, lattice distortions, and surface oxygen vacancies is responsible for the insulator-metal transition of $\text{LaAlO}_3/\text{SrTiO}_3$ with a step function at four LaAlO_3 unit cells and can be controlled by the sample growth conditions and environments.

ACKNOWLEDGMENTS

We acknowledge Ilya Elfimov, Alex Zunger, and Matthew Sherburne for useful discussions and comments on the manuscript. This work is supported by Singapore National Research Foundation under its Competitive Research Funding (NRF-CRP 8-2011-06 and NRF2008NRF-CRP002024), MOE-AcRF Tier-2 (MOE2010-T2-2-121), NUS-YIA, and FRC. We acknowledge the NUS Graphene Center and CSE-NUS computing centers for providing facilities for our numerical calculations. The work at UBC is supported by the Canadian funding agencies NSERC, and CRC as well as the University of British Columbia.

* phyandri@nus.edu.sg

¹ H. Y. Hwang, Y. Iwasa, M. Kawasaki, B. Keimer, N. Nagao, and Y. Tokura, *Nat. Mater.* **11**, 103 (2012).

² C. Cen, S. Thiel, G. Hammerl, C. W. Schneider, K. E. Andersen, C. S. Hellberg, J. Mannhart, *Nat. Mater.* **7**, 298 (2008).

³ C. Cen, S. Thiel, J. Mannhart, and J. Levy, *Science* **323**, 1026 (2009).

⁴ P. Irvin, Y. Ma, D. F. Bogorin, C. Cen, C. W. Bark, C. M. Folkman, C.-B. Eom, and J. Levy, *Nat. Photon.* **4**, 849 (2010).

⁵ N. Nakagawa, H. Y. Hwang, and D. A. Muller, *Nat. Mater.* **5**, 204 (2006).

⁶ T. C. Asmara, A. Annadi, I. Santoso, P. K. Gogoi, A. Kotlov, H. M. Omer, M. R. Motapothula, M. B. H. Breese, M. Rbhausen, T. Venkatesan, Ariando, A. Rusydi, *Nat. Commun.* **5**, 3663 (2014).

⁷ A. Ohtomo and H. Y. Hwang, *Nature* **427**, 423 (2004).

⁸ S. Thiel, G. Hammerl, A. Schmehl, C. W. Schneider, and J. Mannhart, *Science* **313**, 1942 (2006).

⁹ N. Reyren, S. Thiel, A. D. Caviglia, L. F. Kourkoutis, G. Hammerl, C. Richter, C. W. Schneider, T. Kopp, A.-S. Rüetschi, D. Jaccard, M. Gabay, D. A. Muller, J.-M. Triscone, J. Mannhart, *Science* **317**, 1196 (2007).

¹⁰ A. Brinkman, M. Huijben, M. Van Zalk, J. Huijben, U. Zeitler, J. C. Maan, W. G. Van Der Wiel, G. Rijnders, D. H. A. Blank and H. Hilgenkamp, *Nat. Mater.* **6**, 493 (2007).

¹¹ Ariando, X. Wang, G. Baskaran, Z. Q. Liu, J. Huijben, J. B. Yi, A. Annadi, A. Roy Barman, A. Rusydi, S. Dhar, Y. P. Feng, J. Ding, H. Hilgenkamp, T. Venkatesan, *Nat. Commun.* **2**, 188 (2011).

¹² J.-S. Lee, Y. W. Xie, H. K. Sato, C. Bell, Y. Hikita, H. Y. Hwang and C.-C. Kao, *Nat. Mater.* **12**, 703 (2013).

¹³ L. Li, C. Richter, J. Mannhart, and R. C. Ashoori, *Nat. Phys.* **7**, 762 (2011).

¹⁴ J. A. Bert, B. Kalisky, C. Bell, M. Kim, Y. Hikita, H. Y. Hwang and K. A. Moler, *Nat. Phys.* **7**, 767 (2011).

¹⁵ R. Pentcheva and W. E. Pickett, *Phys. Rev. Lett.* **102**, 107602 (2009).

- ¹⁶ M. Stengel, and D. Vanderbilt, Phys. Rev. B **80**, 241103(R) (2009).
- ¹⁷ W.-J. Son, E. Cho, B. Lee, J. Lee, and S. Han, Phys. Rev. B **79**, 245411 (2009).
- ¹⁸ C. Cancellieri, D. Fontaine, S. Gariglio, N. Reyren, A. D. Caviglia, A. Fête, S. J. Leake, S. A. Pauli, P. R. Willmott, M. Stengel, P. Ghosez, J.-M. Triscone, Phys. Rev. Lett. **107**, 056102 (2011).
- ¹⁹ L. Zhang, X.-F. Zhou, H.-T. Wang, J.-J. Xu, J. Li, E. G. Wang, and S.-H. Wei, Phys. Rev. B **82**, 125412 (2010).
- ²⁰ N. C. Bristowe, P. B. Littlewood, and E. Artacho, Phys. Rev. B **83**, 205405 (2011).
- ²¹ Y. Li, S. N. Phattalung, S. Limpijumnong, J. Kim, and J. Yu, Phys. Rev. B **84**, 245307 (2011).
- ²² L. Yu and A. Zunger, Nat. Commun. **5**, 5118, (2014).
- ²³ S. A. Pauli, S. J. Leake, B. Delley, M. Björck, C.W. Schneider, C. M. Schlepütz, D. Martocchia, S. Paetel, J. Mannhart, and P. R. Willmott, Phys. Rev. Lett. **106**, 036101 (2011).
- ²⁴ M. Salluzzo, S. Gariglio, X. Torrelles, Z. Ristic, R. D. Capua, J. Drnec, M. M. Sala, G. Ghiringhelli, R. Felici, and N. B. Brookes, Adv. Mater. **25**, 2333 (2013).
- ²⁵ G. Kresse and J. Hafner, Phys. Rev. B **47**, 558(R) (1993).
- ²⁶ G. Kresse and J. Hafner, Phys. Rev. B **49**, 14251 (1994).
- ²⁷ G. Kresse and D. Joubert, Phys. Rev. B **59**, 1758 (1999).
- ²⁸ A. Balderesch, S. Baroni, and R. Resta, Phys. Rev. Lett. **61**, 734 (1988).
- ²⁹ R. Hesper, L. H. Tjeng, A. Heeres, and G. A. Sawatzky, Phys. Rev. B **62**, 16046 (2000).
- ³⁰ M. Takizawa, S. Tsuda, T. Susaki, H. Y. Hwang, A. Fujimori, Phys. Rev. B **84**, 245124 (2011).
- ³¹ J. Osorio-Guillén, S. Lany, S. V. Barabash, and A. Zunger, Phys. Rev. Lett. **96**, 107203 (2006).
- ³² M. Basletic, J.-L. Maurice, C. Carrétéro, G. Herranz, O. Copie, M. Bibes, É. Jacquet, K. Bouzehouane, S. Fusil, A. Barthélémy, Nat. Mater. **7**, 621 (2008).
- ³³ C. Cancellieri, N. Reyren, S. Gariglio, A. D. Caviglia, A. Fête, J.-M. Triscone, EPL **91**,17004 (2010).
- ³⁴ Z. Q. Liu, C. J. Li, W. M. Lü, X. H. Huang, Z. Huang, S. W. Zeng, X. P. Qiu, L. S. Huang, A. Annadi, J. S. Chen, J. M. D. Coey, T. Venkatesan, Ariando, Phys. Rev. X. **3**, 021010 (2013).